Key Points:
- ETAS modeling results indicate a number of earthquakes with low background probability near the Hutubi underground gas storage facility
- Our earthquake relocations have revealed an unmapped reverse fault with on-fault earthquakes close to the gas injection zone
- Our seismological results suggest that poroelasticity is the mechanism responsible for the observed gas-injection-induced seismicity

Seismological Investigations of Induced Earthquakes Near the Hutubi Underground Gas Storage Facility

Pengcheng Zhou[1] (iD), Hongfeng Yang[1] (iD), Baoshan Wang[2,3] (iD), and Jiancang Zhuang[4] (iD)

[1]Earth System Science Programme, Faculty of Science, Chinese University of Hong Kong, Shatin, Hong Kong, China, [2]School of Earth and Space Sciences, University of Science and Technology of China, Hefei, China, [3]Key Laboratory of Seismic Observation and Geophysical Imaging, Institute of Geophysics, China Earthquake Administration, Beijing, China, [4]Institute of Statistical Mathematics, Tokyo, Japan

Abstract The Hutubi underground gas storage facility in Xinjiang, China, with a maximum gas storage capacity of 10.7 billion m^3, provides a good opportunity to study seismicity potentially induced by the annually cyclic injection and extraction of natural gas. To statistically distinguish induced seismicity from the tectonic background, we investigate the background seismicity probability of each event using the space-time epidemic-type aftershock sequence model and a stochastic declustering method. Our statistical results suggest a potential link between gas injection and two groups of seismicity, with very low background seismicity probabilities during the first and second injection periods in August 2013 and May 2014, respectively. To better understand the earthquake physics, we relocate earthquakes by incorporating a dedicated mobile seismic network after refining the regional 1D velocity model by utilizing an artificial source. After double-difference relocations, those two groups of earthquakes move much closer to the faults bounding the rock storage units and are situated at a depth around 4 km, slightly deeper than the reservoir formation. Focal mechanism solutions of the two largest earthquakes (M_w 2.8 and 3.0) in August 2013 show a possibly unmapped reverse fault gently dipping to the south. Based on our high-resolution earthquake locations, we propose that these on-fault earthquakes are not hydrologically connected with the reservoir formation but are likely induced by poroelastic stress perturbations due to gas injection. Poroelastic stressing can have a larger impact on seismicity rate than pore pressure diffusion at large distances; hence, the distributions and sizes of preexisting faults might play a key role in seismic hazard assessments in our study region.

Plain Language Summary Anthropogenic activities such as underground liquid injection are known to likely cause earthquakes. In comparison, it is unclear whether gas injection may also induce earthquakes, and if so what mechanisms are responsible. Here we conduct a systematic investigation of earthquakes associated with cyclic natural gas injection and extraction in the Hutubi underground gas storage (UGS) facility, Xinjiang, China. Because earthquakes near the UGS have the potential to damage UGS facilities and shatter the caprock integrity, understanding how gas injection may cause earthquakes is important for earthquake physics and also for secure UGS operations. In this study, we statistically identify two groups of gas injection correlated seismicity near the Hutubi UGS. Moreover, their causal links are strengthened by considering closer seismicity-injection distances and depths, based on our results of high-resolution earthquake relocations and estimated source fault geometry. Since these earthquakes are not hydraulically connected with the gas reservoir, they are likely induced by poroelastic stress perturbations due to the gas injection. We suggest that the conditions of preexisting faults play an important role in the potential seismic hazard. Our results also highlight the importance of near-filed seismic monitoring for UGSs to mitigate the risks of earthquakes induced by gas injection and extraction.

1. Introduction

It has long been known that the injection and extraction of fluid can induce earthquakes (Ellsworth, 2013; Healy et al., 1968; Raleigh et al., 1976; Segall, 1989; Suckale, 2009; Yang et al., 2017). Numerous cases associated with liquid injection (e.g., wastewater disposal and hydraulic fracturing) have been globally documented in recent years (e.g., Atkinson et al., 2016; Chen et al., 2018; Holland, 2013; Keranen et al., 2013; Keranen & Weingarten, 2018; Lei et al., 2013; McGarr, 2014). Although gas extraction may induce earthquakes through a poroelastic stress perturbation (e.g., Segall, 1989; Suckale, 2009; Zbinden et al., 2017), relatively
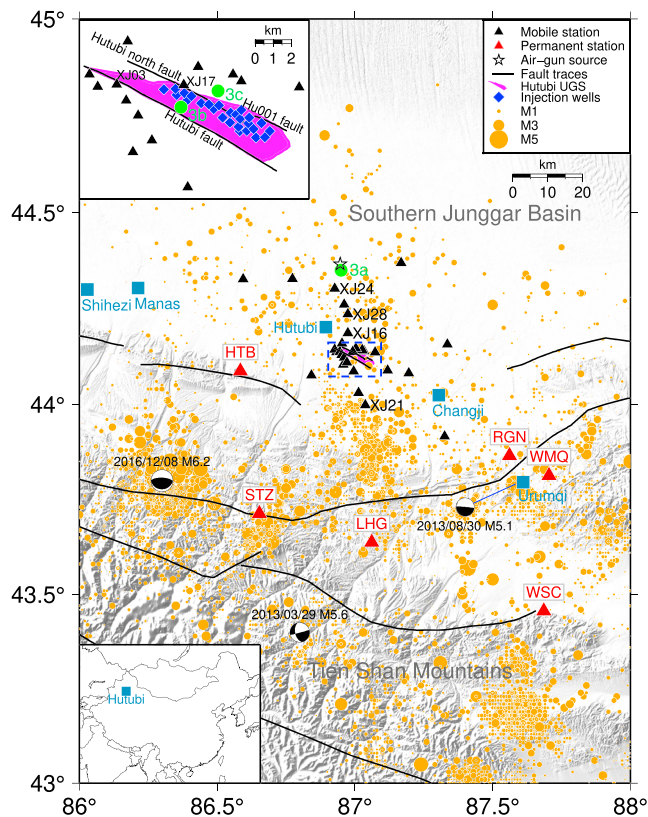
Figure 1. Geographic map of the study region. The lower left inset marks the location of the Hutubi County in China. The main map shows China Earthquake Administration (CEA) catalog earthquake hypocenters (orange dots) between January 2009 and June 2018, the Hutubi UGS (magenta), seismic stations (red triangles: permanent; black triangles: mobile), air-gun source (black open star), and fault traces (black lines, Deng et al., 2003). The occurrence time and focal mechanisms (Global Centroid Moment Tensor solutions) are shown for three earthquakes with a magnitude larger than *M*5. Cities and their names are colored in sky blue. Upper left inset: The zoom-in of the blue dashed rectangular area, with injection wells (blue diamonds) and three mapped faults dipping to the south. The green filled circles (3a–3c) show three different locations of the same earthquake in Figure 3. UGS = underground gas storage.

fewer cases of earthquakes induced by gas injection have been documented (Foulger et al., 2018; Wilson et al., 2017), probably because only a small number of gas injection cases have been seismically monitored. A notable case was the Castor project in Spain. This project was shut down after triggering hundreds of small earthquakes (Cesca et al., 2014; Juanes et al., 2017), although it is still debated whether its sudden suspension unexpectedly promoted the occurrence of the largest M_w 4.3 earthquake (Grigoli et al., 2017). Understanding how gas injection may cause earthquakes is not only important for earthquake physics (Galis et al., 2017) but will also enable underground gas storage (UGS) facilities, where the annual cyclic injection and extraction is conducted to meet seasonal variation in demand for gas, to be operated more safely (Yang et al., 2017). To meet the rapidly growing demand for natural gas, an attractive green energy source, large UGSs have been constructed in many countries, and it is therefore important to understand how they might be damaged or affected by induced earthquakes. Here we systematically investigate earthquakes that occurred near a UGS facility in Hutubi, Xinjiang, combining a newly installed dense seismic network with permanent stations, to distinguish seismicity related to the UGS facility and to assess the seismic hazards.

Located in the southern margin of the Junggar Basin, the Hutubi UGS facility was originally a natural gas field that was depleted in 2009. It was subsequently converted into a UGS with a storage capacity of 10.7 billion m^3, the largest of its kind in China. Shortly after the first injection on 9 June 2013, a sequence of earthquakes occurred in the vicinity of the UGS, including two earthquakes with local magnitudes (M_L) larger than 3 (Figure 1, Yang et al., 2017). Tang et al. (2018) have detected and located earthquakes from 2013 to 2015 in the region using the sparse Xinjiang Seismic Network and found that most of the earthquakes occurred in the first two injection periods and were distributed in two shallow clusters (focal depth < 2 km). Based on the time delays between the occurrences of the earthquakes and the abrupt changes in the gas injection rate and well pressure, Tang et al. (2018) concluded that these earthquakes were induced by both pore pressure changes and poroelastic responses, which led to the failure on nearby faults that were governed by the rate- and state-dependent friction law (Dieterich, 1979). However, in the rate-state-frictional formulation, velocity strengthening (aseismic) behavior is often found at shallow depths (<2 km, Blanpied et al., 1998; Marone, 1998), where earthquakes are not anticipated to occur and faults presumably slip aseismically. If indeed earthquakes are shallower than 2 km and are induced as suggested by Tang et al. (2018), pore pressure changes cannot be the responsible mechanism because the injected gas is sealed by the caprock that is located at ~ 3 km in depth (Hu et al., 2010; Pang et al., 2012). Furthermore, the Hutubi UGS is located in the Junggar Basin with low seismicity levels, but earthquakes are quite active in the Tien Shan tectonic belt adjacent to the Hutubi UGS. It is therefore by no means certain that these earthquakes were directly induced by gas injection or extraction.

This study investigates the earthquakes in the vicinity of the Hutubi UGS facility. The major differences between our approaches and those taken by Tang et al. (2018) are as follows. We conduct a statistical analysis of the local earthquake catalog to identify the seismicity rate changes and to highlight earthquakes that can be distinguished from the background seismicity. To obtain high-resolution earthquake locations, we derive a new local velocity model using an artificial air-gun source located ~30 km north to the UGS and a newly deployed seismic network since 2013. The inferences drawn directly from statistical analysis and earthquake relocations can provide comprehensive evidence on whether the observed seismicity is linked with gas injection/extraction or not. We also derive focal mechanism solutions for the two

largest earthquakes, which provide independent information on the fault geometry. Based on our high-resolution earthquake locations and focal mechanism solutions, we are able to determine the hydraulic connectivity of the faults to the reservoir formation so as to infer the mechanisms responsible for these earthquakes.

2. Tectonic Setting, UGS Operations, and Data

2.1. Tectonic Setting

Hutubi is located in the southern Junggar Basin in northwestern China (see Figure 1), adjacent to the Tien Shan (also called Tian Shan or Tianshan) Mountains. Originally formed in the Paleozoic, the Tien Shan range is actively uplifting, with fold-and-thrust belts currently deforming near the foreland of the southern Junggar Basin (Deng et al., 2003; Guan et al., 2012). GPS data show that the north-south shortening is proceeding at a rate of 2~5 mm/year in our study region (Qiao et al., 2018). As the region is close to the northern Tien Shan fold-and-thrust belts, many tectonic earthquakes with magnitudes larger than M3 have occurred there (Lu et al., 2017), including a magnitude M6.2 earthquake that struck the Hutubi County on 8 December 2016 (see Figure 1). Many other small earthquakes have also occurred near Hutubi, making it difficult to differentiate tectonic background earthquakes from induced earthquakes by anthropogenic activities (Figures 1 and 2).

The Hutubi UGS used to be a gas field discovered in 1996 and is related to the Hutubi anticline, cut by two parallel northwest trending faults (Hu et al., 2010) with low levels of historical seismicity with magnitudes over M3 within 15 km (Yang et al., 2017). Seismic and geologic surveys mapped another thrust fault beneath the reservoir depth near the northeastern boundary of the UGS (Figure 1, Cao, 2013; Pang et al., 2012). The three faults shared similar strikes in the northwest direction (Figure 1) and identical dip angles of around 20° dipping to the south as we estimated from the documented seismic profiles (Cao, 2013; Pang et al., 2012; Jiang et al., 2019).

The main gas reservoir is characterized by Paleogene sandstone from the Ziniquanzi formation, with porosity and permeability ranging from 5.3% to 22.4% and 0.201×10^{-15} m^2 to 131×10^{-15} m^2, respectively (Hu et al., 2010). The reservoir formation (i.e., Hutubi UGS) is ~3.5-km deep at its center, with an average thickness of 200 m (Cao, 2013). The overlying mudstone is the Anjihai formation and acts as an excellent regional caprock for the gas reservoir, preventing gas leakage upward (Hu et al., 2010; Pang et al., 2012). We discuss hypocenter locations and focal depths relative to subsurface formations in section 6.2.

2.2. UGS Operations

The construction of the Hutubi UGS facility began in July 2011. It was built on the basis of the Hutubi gas field, where gas production was completely shut down in September 2012. And the Hutubi UGS went into operation on 9 June 2013 (Figure 2a). The Hutubi UGS was designed with a peak storage capacity of 10.7 billion m^3 and was intended to play a key role in the West-East Gas Pipeline Network. The annually cyclic injection and extraction of high-pressure gas caused observable ground deformation and stress changes. Qiao et al. (2018) observed subsidence and uplift values near the Hutubi UGS varied from −13.7 to 15.5 mm, respectively. Estimated monthly pore pressure changes ranged from −0.071 to 0.093 MPa and went beyond the critical thresholds required to induce small earthquakes (Qiao et al., 2018).

Newly drilled wells (blue diamonds in the upper left inset in Figure 1), conducting gas injection in summer and gas extraction in winter, are distributed within the Hutubi UGS (the magenta polygon in Figure 1), with depths varying between 3.0 and 3.8 km (Chen et al., 2016). During the first two injection/extraction periods, the daily total injection and extraction rates peak at about 10^7 m^3 from April to October and 4×10^6 m^3–8×10^6 m^3 from November to March (the next year), respectively (Figure 2a, Tang et al., 2018). Under continuous gas injection, the wellhead pressure gradually increases, climbing to about 28 MPa (Figure 2b). Each injection period is followed by a shut-in period, during which no injection or extraction is performed. Under continuous gas extraction, the wellhead pressure gradually drops to lows of about ~12 and ~16 MPa during the first and second gas extraction periods, respectively (Figures 2a and 2b). In section 6.3, we discuss the links between well operation data (also see Tang et al., 2015, 2018) and our relocated earthquake sequences.
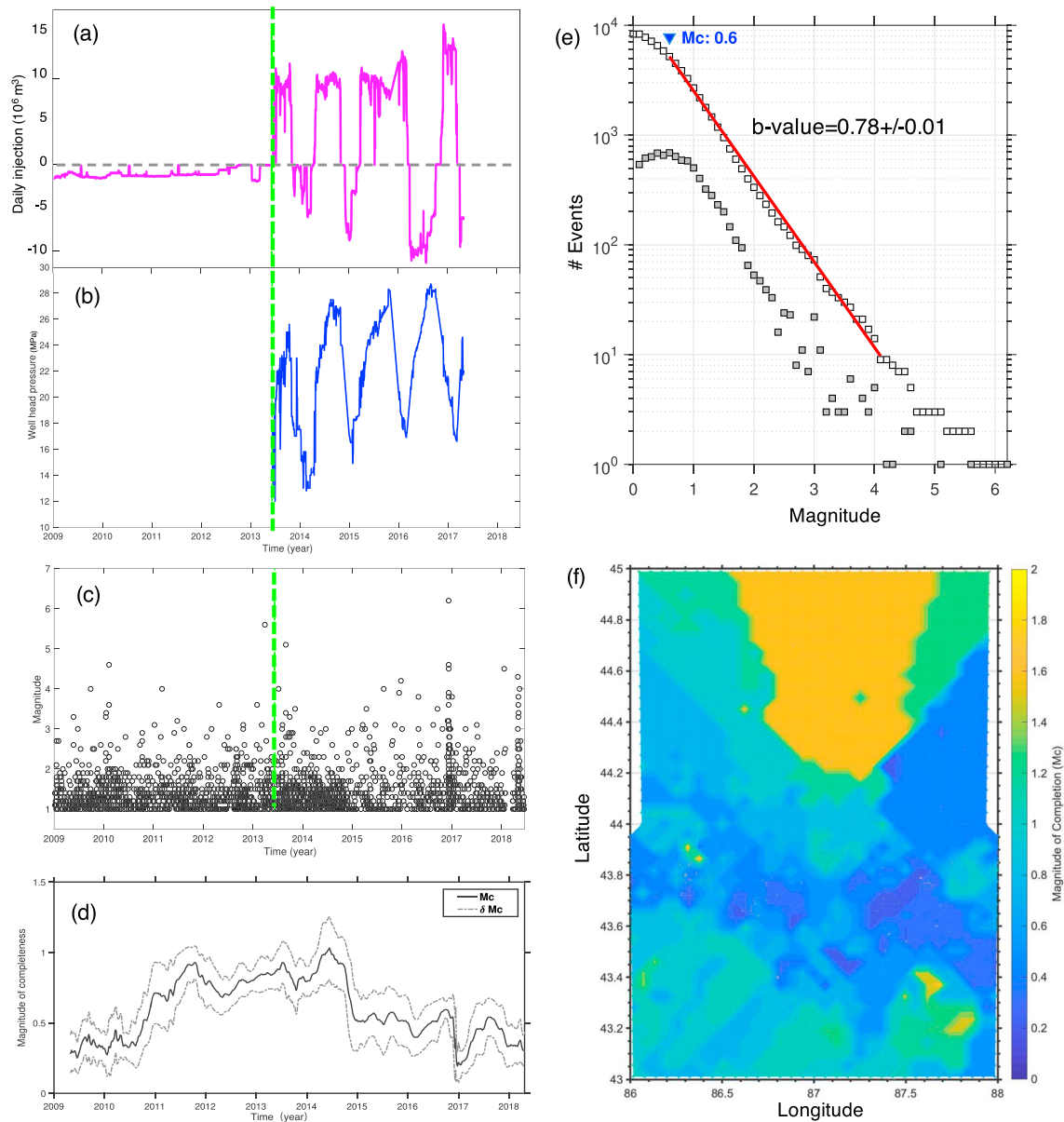
Figure 2. UGS operation and catalog analysis. The green dashed line denotes the initial operation time of the Hutubi UGS facility. (a and b) The daily gas injection/extraction volume data from January 2009 to April 2017 and wellhead pressure data from June 2013 to April 2017. (c) Earthquakes with a magnitude over M_L 1 versus time. (d) Earthquake magnitude completeness (M_c) calculated using ZMAP in time. (e) Frequency-magnitude distributions and best-fitted M_c and b value. (f) Geographic distribution of M_c calculated using ZMAP. UGS = underground gas storage.

2.3. Data
2.3.1. Earthquake Catalog

To statistically distinguish induced seismicity from tectonic seismicity in section 3, we select a study region bounded by longitudes 86° and 88° and latitudes 43° and 45° during 2009 and June 2018 to reduce the spatial edge effects in parameter estimations and also to ensure sufficient samples (Seif et al., 2017). More than 8,300 earthquakes (orange dots in Figure 1) were reported within this area by the China Earthquake Administration, with magnitudes down to M_L 0.1.

The selected spatial range is shown in Figure 1. To avoid magnitude completeness (M_c) heterogeneity problems in seismicity studies, we need a careful selection of minimum magnitude threshold to perform statistical analysis. To compute M_c in time, we use a moving window approach and select the sample window as
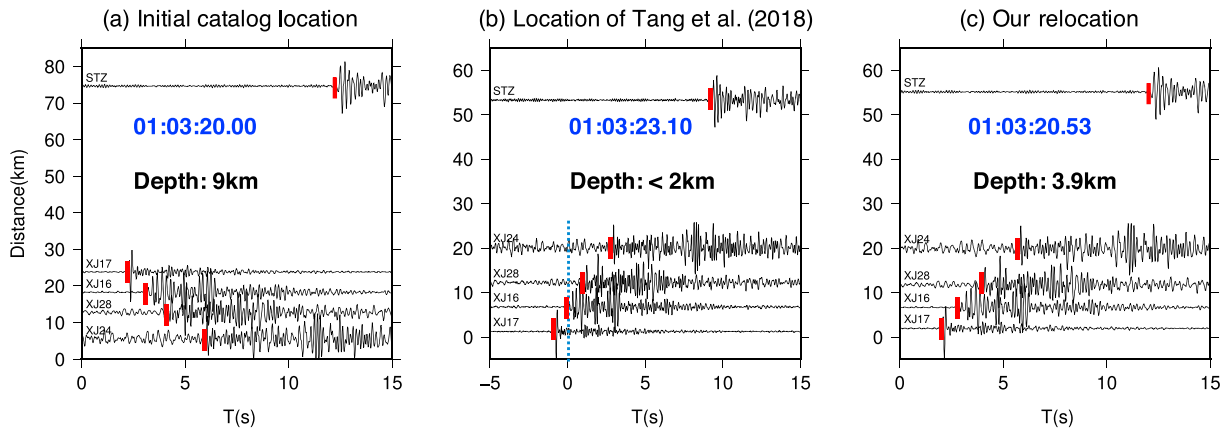
Figure 3. Comparison of earthquake locations. An example showing three different location precisions of the same earthquake. Hypocenter locations (Figures 3a–3c) can be seen from Figure 1 (green filled circles), and depths are labeled as text on each panel. The origin time of the earthquake is shown as blue text in each panel on the date 10 May 2014. The traces plotted are vertical components, filtered between 1 and 8 Hz. Red bars denote manually picked *P* wave arrival times. XJ16, XJ17, XJ24, and XJ28 are four stations in the mobile network, and STZ is a permanent station (red triangle in Figure 1). In each panel, the *y*-axis indicates the increasing source station distance from the epicentral location and the *x*-axis indicates the time relative to the origin time. (a) The waveform profile of the earthquake by assigning the initial catalog location. (b) The waveform profile of the earthquake by assigning the relocation by Tang et al. (2018). The blue dotted line marks the origin time. Given a reliable location, *P* waves are expected to arrive later than the origin time and later with increasing source-station distance. Therefore, location errors of the initial catalog and Tang et al. (2018) can be implied from Figures 3a–3b. (c) The waveform profile of the same earthquake by assigning our relocation (see section 4.2).

500 events overlapping with 50 events. We compute M_c in each window and assign the corresponding time as the middle of the window. Our calculated results indicate that M_c changes as a function of time, with a peak value below 1.02 (Figure 2d). So a value of 1.0 is chosen on the conservative side (Figure 2c). The maximum curvature technique is based on the Gutenberg-Richter power law assumptions of the cumulative frequency-magnitude distribution (Figure 2e). We also map M_c (Figure 2f) within the same spatial range as shown in Figure 1 by applying the maximum curvature technique using the tool ZMAP (Wiemer, 2001; Wiemer & Wyss, 2000). For the analysis, a constant number of events per sample (150) is used.

The initial earthquake catalogs were routinely generated by Xinjiang Seismic Network permanent stations at least several tens of kilometers away from the Hutubi UGS (see Tang et al., 2018), enabling the locations of the earthquakes to be roughly plotted (Figure 3). To better distinguish induced seismicity from tectonic seismicity based on high-resolution earthquake locations in section 4.2, we conduct our analysis by considering a smaller region and a shorter period. To ensure not missing important events and also to exclude distant events in relocation procedures, we focus on a moderate size region within ~50-km distance to the Hutubi UGS. Here our study area is bounded by longitudes 86.5° and 87.5° and by latitudes 43.6° and 44.5°, and our period of study is between June 2013 and December 2015.

2.3.2. Seismic Data

To complement the sparse permanent seismic network (red triangles in Figure 1) and the azimuth gap in the north, we deployed a mobile network (black triangles in Figure 1), consisting of 38 mobile seismic stations in 3 stages, starting in 2013. The permanent stations are spaced around 50 km apart on average, while the mobile stations are on average 3 km apart, and in some cases as close as 1 km. Denser azimuthal coverage guarantees more accurate locations of earthquakes, especially for small ones near the mobile network. We collect the continuous waveform data on mobile stations and request the event waveform data on permanent stations closer than 200 km to the Hutubi UGS facility between June 2013 and December 2015 (Zheng et al., 2010). The sampling rate in the permanent and mobile stations is identical, at 100 samples per second, except in the case of station XJ19, which had a rate of 250 samples per second. We discard the data from the 10 mobile stations ringing the Tien Shan with poor signal-to-noise ratios and the permanent station HTB suffering from clock errors, and finally, we use 28 mobile stations and 14 permanent stations within 200 km of the Hutubi UGS to manually pick *P* wave and *S* wave phase arrival times. In section 5, we calculate the focal mechanisms and the moment magnitudes of the two largest earthquakes in the study period.

2.3.3. Active Source

In addition to the earthquake data, the Hutubi air-gun source, transmitting seismic signals with energies equal to a magnitude M_L 0.9 earthquake by a single shot, was installed about 30 km north of the Hutubi UGS in 2013 (see details in Tang et al., 2018). The air-gun signals can be clearly observed at seismic stations over distances of 400 km after stacking of 100 air-gun shots (Yang, 2015; Chen et al., 2017, Figure S1 in the supporting information), which enable us to refine and validate our regional velocity model in section 4.1.

3. Identification of Low Background Probability Seismicity by Using the ETAS Model

3.1. Methodology: The ETAS Model

To statistically distinguish between induced seismicity and tectonic background seismicity, we fit the space-time epidemic-type aftershock sequence (ETAS) model to the observed seismicity and calculate the background probabilities for each event in selected space-time-magnitude range, by making use of the ETAS model-based stochastic declustering method (Jia et al., 2018; Zhuang et al., 2002, 2005). Combining the Omori-Utsu law, productivity law, and Gutenberg-Richter law, the ETAS model is a powerful and widely used tool for spatiotemporal seismicity analysis (Ogata, 1998; Ogata & Zhuang, 2006). The total seismicity rate is described as contributions of tectonic background seismicity and triggered aftershocks. For injection-induced seismicity cases, the total seismicity rate is described as contributions of tectonic background seismicity and induced seismicity (Lei et al., 2013).

In the space-time ETAS model (Jia et al., 2018; Ogata, 1998; Ogata & Zhuang, 2006), the total occurrence rate is written as the sum of the rate triggered by all preceding earthquakes and a background seismicity rate $\mu(x,y)$

$$\lambda(t,x,y) = \mu(x,y) + \sum_{\{i:t_i<t\}} \kappa(m_i)g(t-t_i)f(x-x_i,y-y_i;m_i) \tag{1}$$

where $\kappa(m)$ is the productivity, describing the numbers of earthquakes induced by an earthquake with magnitude m. $g(t)$ is the time probability density function, and $f(x,y;m)$ is the spatial probability density function. The detailed representations are as follows:

$$\kappa(m) = Ae^{a(m-m_c)}, m \geq m_c \tag{2}$$

$$g(t) = \frac{p\text{-}1}{c}\left(1+\frac{t}{c}\right)^{-p} \tag{3}$$

$$f(x,y;m) = \frac{q\text{-}1}{\pi De^{\gamma(m-m_c)}}\left[1+\frac{x^2+y^2}{De^{(m-m_c)}}\right]^{-q} \tag{4}$$

where m_c (in equations (2) and (4)) is the low cutoff magnitude. We can iteratively estimate the ETAS parameters (see details in Ogata & Zhuang, 2006) A, α, c, p, D, q, and γ by the maximum likelihood method given initiating parameters and a complete catalog.

3.2. Methodology: ETAS Model-Based Stochastic Declustering

ETAS model describes how aftershocks tend to cluster around a mainshock: the whole process includes two components: the background events (independent occurrence) and the aftershocks (clustered). Background events are those that occur independently, but likely result from a similar process, such as tectonic loading. Aftershocks are induced or triggered by previous earthquakes. The stochastic declustering aims to separate the contributions from the two components to estimate the probability of each event being a background event (Zhuang et al., 2005). The uncertainty in the declustering outputs can be evaluated by incorporating many simulated copies of the declustered catalog. Therefore, the stochastic declustering method gives a more reliable estimation of clustering than other conventional declustering processes (Jia et al., 2018; Zhuang et al., 2005).
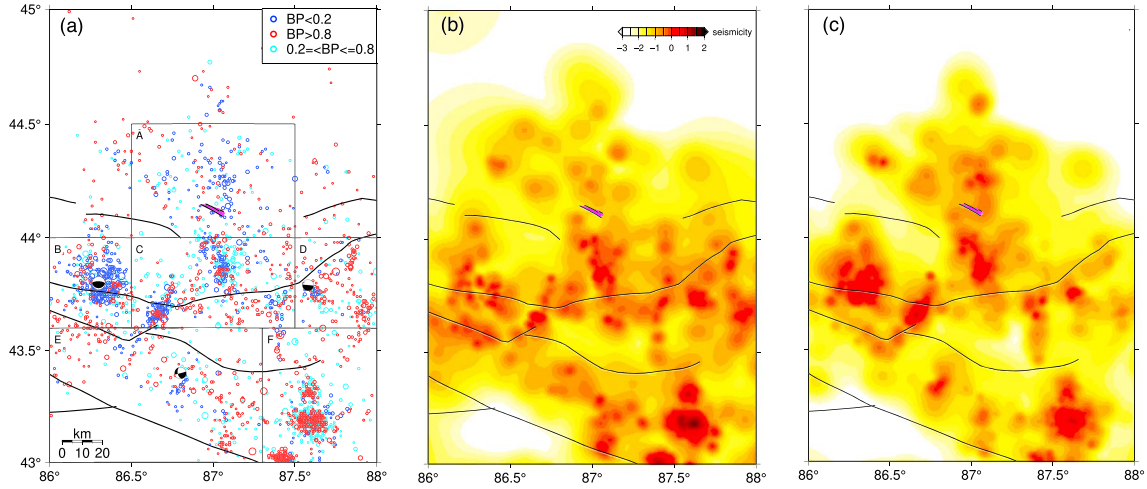
Figure 4. ETAS modeling results. (a) Illustration of rectangular region classifications A–F. BP means background probability. Background seismicity probabilities of ETAS modeling results are represented in circles with high (red, BP > 0.8), medium (cyan, 0.2 = <BP < = 0.8), and low (blue, BP < 0.2) values. The magnitude ($M_L \geq 1$) is denoted by circle sizes. (b) Estimated background seismicity rate (in the unit of events/degree^2/year) in the logarithm scale. The black lines represent the major faults in the study region. (c) The estimated clustered seismicity rate following similar conventions as Figure 4b. ETAS = epidemic-type aftershock sequence.

The background probability quantifies how likely an event is a background event (Zhuang et al., 2005), ranging from 0 (purely background) to 1 (completely triggered). After we estimate the ETAS model parameters, we are able to calculate the background probability of each event φ_j, which is represented by the ratio of the background seismicity rate $\mu(x_j, y_j)$ and total seismicity rate $\lambda(t_j, x_j, y_j)$ of the jth event:

$$\varphi_j = \frac{\mu\left(x_j, y_j\right)}{\lambda\left(t_j, x_j, y_j\right)} \tag{5}$$

where t_j, x_j, y_j are the event occurrence time and location of the jth event.

A simple threshold for differentiating is to categorize events with background probabilities larger than 0.8 as background seismicity, while events with background probabilities lower than 0.2 are more likely induced or triggered seismicity (Jia et al., 2018). In Figure 4a, the circles indicate the categorized seismicity.

To describe probabilities of seismicity not belonging to the background, we introduce the clustering probability (Zhuang et al., 2005):

$$\rho_j = 1\text{-}\varphi_j \tag{6}$$

To inspect clustered seismicity rate changes, we use the formulation raised by Zhuang et al. (2005) to calculate the cumulative clustered probabilities of earthquakes $C(t)$ occurring at time t:

$$C(t) = \sum_{t_j < t} \rho_j \tag{7}$$

If the slope of $C(t)$ decreases, a low stress change is expected. Otherwise, if the slope of $C(t)$ increases, a high stress change is required (Mignan et al., 2018). In Figure 5, the black solid lines in each panel correspond to $C(t)$ plots.

3.3. Results

We pick a 2° × 2° region (Figure 4) centered on the Hutubi UGS for model fittings. We choose m_c=1.0 (see section 2.3.1) as a magnitude threshold to model parameter estimation. We initiate the starting parameters and then estimate the ETAS model parameters using the maximum likelihood method (Zhuang et al., 2002).
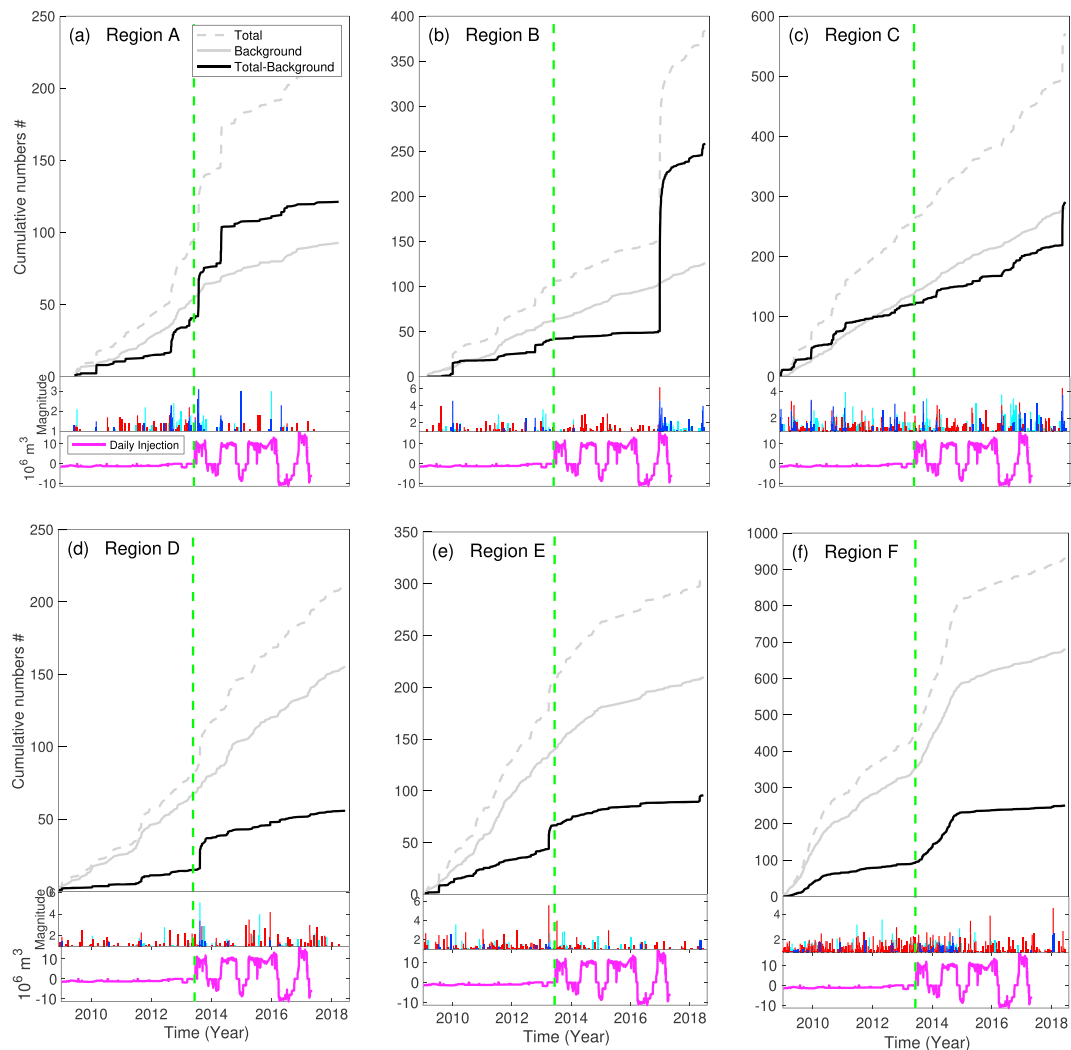
Figure 5. Cumulative curves of events. (a-f) Upper panels: cumulative curves of the background and total events in regions A–F are plotted in solid and dashed gray, respectively. The corresponding cumulative clustered events (subtracting the background from total) are shown in black curves. Middle panels: magnitudes against times. The colors correspond to the conventions in Figure 4a. Bottom panels: daily gas injection/extraction volumes against times.

And finally, we estimate model parameters as $A = 0.03438$ (events), $c = 2.2992\times10^{-3}$ (day), $\alpha = 1.047$ (per meter), $p = 1.072$, $D = 9.725\times10^{-4}$ (degrees squared), $q = 1.862$, and $\gamma = 0.1662$ (per meter).

On the assumption that events with background probabilities larger than 0.8 are more likely to infer a categorization of background seismicity, while lower than 0.2 are more likely to infer a categorization of induced or triggered seismicity (Jia et al., 2018), the blue circles in Figure 4a are likely to be induced or triggered. For instance, we identify two groups of earthquakes in 2013 and 2014 in region A (Figure 4a) that show high probabilities of induced seismicity types (the middle panel in Figure 5a). To demonstrate the power of the declustering method, we show the background seismicity rate and clustered seismicity rate on a logarithmic scale in Figures 4b and 4c, which show very different patterns.

To investigate the seismicity behaviors in space and time, the study region is divided into six subregions bounded by rectangle after considering local tectonic structures and hypocenter distributions (Figures 1 and 4a). To determine the bounding choices, we test different combinations by using ZMAP (Wiemer, 2001; Wiemer & Wyss, 2000). The bounding box for subregion A is selected by considering a distance of about 40 km to the Hutubi UGS but with a bounding distance of 10 km to the south (latitude 44° in Figure 4a). We observe scattering seismicity and clustering seismicity above and below the latitude 44°

line, respectively. Therefore, we intend to isolate the seismicity above the latitude 44° line. Such strategies, by separating spatially scattering and clustering seismicity, can also explain our bounding choices of the lines between subregion C and subregions B–F. The seismicity cluster in subregion B is mostly influenced by the centering Hutubi 2016 M6.2 earthquake, so we just bound the cluster with a small box. For regions A–C, the clustered seismicity (blue bars in Figures 5a–5c) is significant. While, for regions D–F, background seismicity (red bars in Figures 5d–5f) dominates. The region F (Figure 5f) is characterized by very concentrated hypocenters within several clusters.

For region A, we observe $C(t)$ slope changes shortly after the UGS went into operation (Figure 5a). The slope of $C(t)$ curve exhibits two sharp increases in time, corresponding to two groups of earthquakes that occurred in August 2013 and May 2014, respectively (black solid line in Figure 5a). However, we observe much less seismicity after 2015 in region A. The fraction of clustered seismicity in region A begins to increase above 50% of the total seismicity (top panel in Figure 5a). This feature, that clustered seismicity but not aftershocks of large earthquakes dominated over time, is very different from behaviors in other regions. For instance, clustered seismicity rates indicated in Figure 5b are dominated by aftershocks of the 2016 M6.2 Hutubi earthquake. In region C (see Figure 5c), the closest region to the south of the Hutubi UGS, we observe that $C(t)$ slope slightly increases shortly after the UGS beginning its operation, with the fraction of clustered seismicity beginning to drop below 50% of the total seismicity (Figure 5c). An increase of clustered seismicity is also observed (Figures 5a–5c) before the injection activity started at the UGS (September 2012, in line with the observed seismicity increase). The shutdown of production wells and/or drilling activities at the Hutubi UGS may be speculated as a contributor for the seismicity increase (Figure 5a), but the detailed investigation is beyond the scope of this paper. For regions B, D, and E (see Figures 5b, 5d, and 5e), the tectonic background seismicity is the main contributor to the total seismicity, with clustered seismicity rate changes relating to the aftershocks of large tectonic earthquakes. For region F (see Figure 5f), suspected mining activities might have produced some of the recorded events (Tang et al., 2017), but they are unlikely to have been related to the Hutubi UGS activities due to their relative remoteness from the injection wells.

Statistical analysis is not enough to resolve the responsible physical mechanisms for the potentially induced seismicity. To conduct a physics-based seismological analysis, we need high-resolution earthquake locations and detailed source information. Based on the spatiotemporal seismicity features of our fitted ETAS model and background seismicity rate changes, we select a rectangular area by including subregions A and C to conduct earthquake relocations (Figures 4a and 5). We consider two major factors in selecting the target study region and study period. One is to guarantee to cover a sufficient amount of seismicity associated with gas injection/extraction periods. The other is to ensure a small region and a short study period, to exclude significant tectonic background seismicity. Based on the detailed inspections of those subregions, we select a spatial range bounded by longitudes 86.5° and 87.5° and latitudes 43.6° and 44.5°, covering regions A and C, and a timespan from June 2013 to December 2015.

4. Earthquake Relocations

High-resolution locations including focal depths are vital for distinguishing between induced earthquakes and tectonic earthquakes. We therefore first calibrate the regional velocity model in section 4.1, since an oversimplified velocity model might play a role in biasing earthquake locations for the Hutubi region (Figures 3a and 3b). We then obtain high-resolution earthquake relocations in section 4.2 by incorporating the mobile station data and our best-estimated velocity model.

4.1. Velocity Model Refinement

We validate the regional 1D P wave velocity model after revising two previous models as shown in Figure 6 (Ji et al., 2017; Sun et al., 2012). Sun et al. (2012) use earthquake data to calibrate velocity models suitable for the northern part of the Tien Shan Mountains and the southern Junggar Basin; their determined model ensured that the relocated numbers of earthquakes reached its maximum and the relocated epicenters agreed best with local deep structures. Ji et al. (2017) inverted the S velocities for the northern Hutubi from surface wave dispersion curves of stacked air-gun signals and estimated P velocities using P/S ratios; their final inverted model confined well on velocities shallower than 1-km depth.
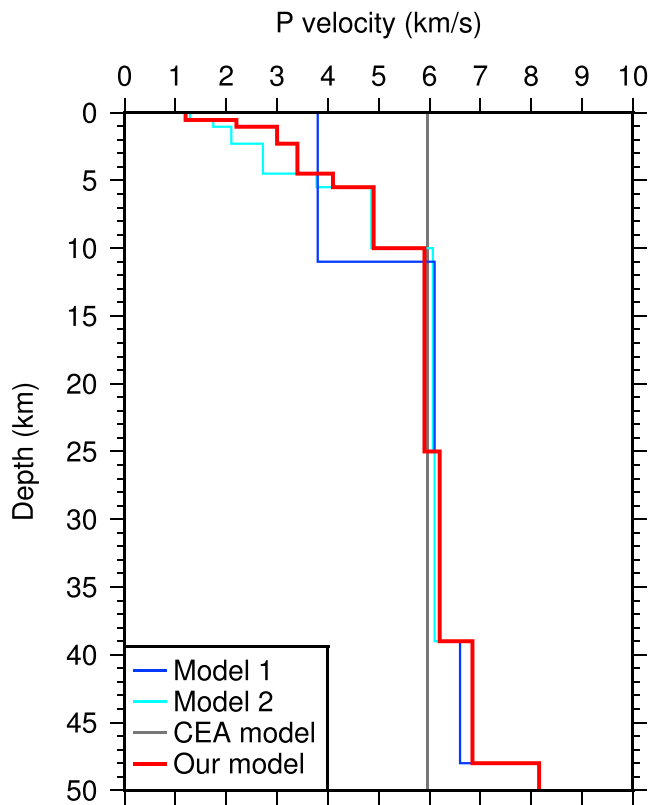
Figure 6. Different velocity models. Model 1 is modified from Sun et al. (2012) and Model 2 is modified from Ji et al. (2017). Our best-estimated model is plotted in red. The model routinely used by CEA is plotted in gray (Sun et al., 2012). CEA = China Earthquake Administration.

Here we fit our picked *P* arrivals of stacked air-gun signals (Figure S1) to velocity model calibration using a grid searching approach. A total of 21 permanent and mobile stations are selected with clear *P* arrivals. We require monotonically increasing velocity with depth, and layered depths are fixed to values defined by the model of Ji et al. (2017). For the *P/S* ratio uncertainties, we allow slight changes in velocities above 1.05 km. The documented two velocity models (Figure 6, Sun et al., 2012; Ji et al., 2017) either overestimate or underestimate the *P* velocities for shallow structures, respectively, and exhibit significant travel time bias, especially where the mobile stations are concerned. Therefore, we set broader ranges above the upper 10 km than the deeper parts bounded by the two documented models.

In the grid search, we choose a velocity bin of 0.1 km/s and define the travel time residuals as $T_{obs} - T_{cal}$, in which T_{obs} is the observed first *P* arrival time and T_{cal} is the predicted time from the given velocity model. In the first step, we filter out those models that produce overly significant results on a subset of the stations. The mobile stations nearest to and furthest from the center of the air-gun source are XJ24 and XJ21, at distances of 7 and 41 km, respectively. To avoid bias from these two stations, we add another station XJ03, 25 km away from the air-gun source. We retain those models that produce residuals falling between a range of −0.5 and 0.5 s on the three selected stations for the next step determination. In the second step, we apply a more rigid residual range of 0.05 s produced by each velocity model. We accept those models that produce residuals falling between −0.05 and 0.05 s for at least 15 stations. After we take these steps, the number of acceptable velocity models finally falls to 31 (Figure S2). Of the finally acceptable velocity models (Figure S2), we select our best-estimated velocity model (red curve in Figures 6 and S2) with the smallest velocity values for the top layer above 500 m, where very low S wave velocity values were found in the ambient noise tomography study of the Hutubi UGS region (Wang et al., 2018). Compared with Ji et al. (2017), we slightly elevate the velocity values for the shallower depths between 0.5 and 5.5 km (red curve in Figure 6).

4.2. Earthquake Relocations

We use hypoinverse (Klein, 2002), an absolute location method, to refine earthquake locations and apply the distance-weighting scheme with full weights assigned to stations closer than 150 km. To validate our best-estimated velocity model, we use hypoinverse to locate the air-gun source using records on stations closer than 200 km. Compared with the known location of the air-gun source within a water pool on the ground, hypoinverse refined locations show a horizontal offset of around 400 m to the south-east (Figure 7a) and relocated depths fall between 1.5 and 2.0 km.

We invert for hypocenters using a total of 2484 *P* and 1557 *S* arrival picks on 42 stations with epicentral distances within 200 km. Here we require at least four picks for a single event and use a value of 1.75 as a constant *P* to *S* velocity ratio. We are able to locate 313 out of 560 catalog earthquakes (Figure 7a) using hypoinverse by applying our best-estimated velocity model (red curve in Figure 6). The horizontal and vertical average location precision improves to 1.56 and 2.56 km, respectively.

Interestingly, some hypocenters migrate from north to south after the hypoinverse refined locations. We expect such improvements due to the incorporation of our best-estimated velocity model and mobile stations with a better azimuthal coverage. China Earthquake Administration routinely generates earthquake catalog using a velocity value of around 5.9 km/s for all depths (gray curve in Figure 6, Sun et al., 2012), much faster than ours. The available permanent stations are mainly located near the Tien Shan Mountains in the south. An earthquake occurring in the north is expected to move closer to the permanent stations to optimize the travel time fittings.
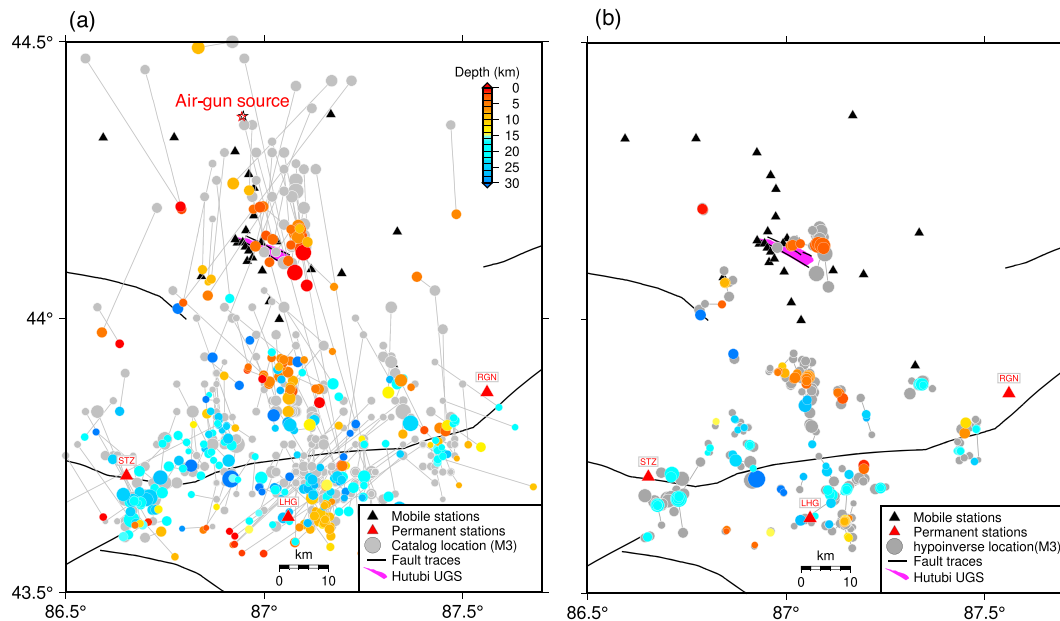
Figure 7. Map of refined locations and relocations. Colors indicate the earthquake depths. (a) Initial catalog locations (gray filled circles), with links (gray lines) of the corresponded hypoinverse refined locations (colored filled circles) are displayed. The air-gun source true location (black open star) and its hypoinverse refined location (red open star) show an offset of 400 m. (b). Gray filled circles show hypoinverse locations with gray lines linking the corresponded hypoDD relocations (colored filled circles).

We find depth contrasts between hypoinverse located earthquakes near the Hutubi UGS in the north and those near Tien Shan in the south. The Moho depth of the southern Junggar Basin near our study region is approximately 50 km (Li et al., 2016). Therefore, earthquakes with depths exceeding approximately 35 km are likely to be associated with crustal structures (Sun et al., 2012).

To reduce the velocity model dependence, we apply the double-difference location approach hypoDD (Waldhauser & Ellsworth, 2000) to 313 hypoinverse refined earthquake locations. We band-pass filter event waveforms between 1 and 8 Hz and perform cross-correlations to obtain differential times, with a cross coefficient cutoff threshold of 0.5. Both P wave and S wave phase data are used in generating differential times. The events are linked using a maximum separation of 15 km, and the minimum number of observations is set to 5. A total of 8,354 differential times are selected based on the above criteria. Consequently, we are able to relocate 167 out of 313 earthquakes. An average root-mean-square of 0.09 s corresponds to a reduction of 75% between the hypoDD relocation and hypoinverse locations (Figure S3). Average horizontal and vertical errors drop to 0.14 and 0.12 km after hypoDD relocations, respectively (Figure S4). The relative location precision improves by 1 order of magnitude compared to the absolute location results.

Due to the depth and proximity to the injection wells located within the Hutubi UGS, here we focus on the relocated earthquakes within a distance of 10 km to the Hutubi UGS (Figure 8a). Hence, we have two groups of earthquakes (see Figure 8) during the first and second gas injection periods, which are suspected to be linked with UGS operations. The first group includes 11 earthquakes outside the Hutubi UGS that occurred within the 5 days between 1 and 5 August 2013 (Figure 8a). The second group includes three earthquakes closer to the Hutubi UGS, which occurred either on 9 or 10 May 2014 (Figure 8a).

In the map view, the group of earthquakes that occurred in August 2013 shows linear trending hypocenters, approximately 2 km from the northeastern boundary of the Hutubi UGS. In section views, most hypocenters fall in the depth range of 3 to 4 km, which corresponds to the Ziniquanzi sandstone formation and basement formation (Figure 8d). In particular, the groups of earthquakes in August 2013 share similar focal depths, probably indicating a low angle fault plane dipping to the south. Focal mechanism solutions provide potentially valuable independent constraints on the fault geometry.
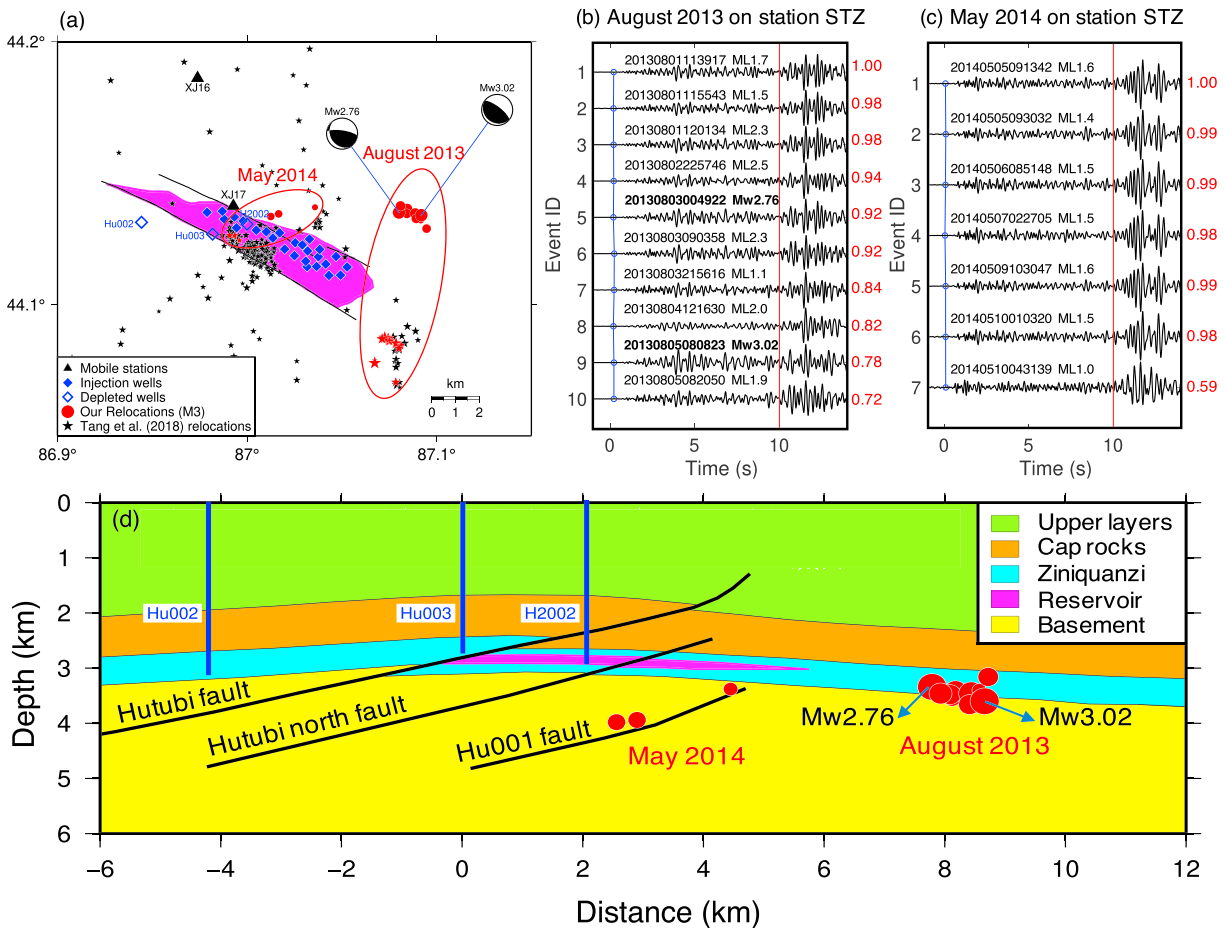
Figure 8. Relocated earthquakes near the Hutubi UGS. (a) The red filled circles and red stars represent two groups of common earthquakes studied by us and by Tang et al. (2018), respectively. Each group is enclosed by the red line, and their occurrence month and the year is labeled as text. Three depleted wells (blue open diamonds) delineate the cross-section in Figure 8d. Waveforms of these two groups of earthquakes are shown in Figures 8b and 8c. North-south component seismograms on station STZ are filtered between 2 and 8 Hz, aligning on the *S* wave arrival times (red), with blue circles marking the *P* arrival times. The occurrence time and magnitude of each trace are shown above each trace. Cross-correlation value with a master event (ID=1) for the S waves (a window containing waveforms 0-2 seconds after the S arrivals) is labeled on the right of each trace. (b) The event IDs of the two largest earthquakes are 5 and 9. (c) Event IDs 5–7 are three relocated earthquakes in May 2014. Event IDs 1–4 are another four catalog earthquakes in May 2014, which were initially located to the north of the UGS and lost in relocation procedures. (d) Relocated earthquakes (following the same conventions in Figure 8a) are projected onto the geological formations, corresponding to the cross-section denoted by three depleted wells in Figure 8a. The reservoir formation (i.e., Hutubi UGS) is colored in magenta. UGS = underground gas storage.

5. Focal Mechanism Determination

Here we implement focal mechanism inversions of two earthquakes with magnitude M_L 3.0 and M_L 3.1 (Figure 8a). We calculate the focal mechanisms using the Cut and Paste (CAP) method (Zhao & Helmberger, 1994; Zhu & Helmberger, 1996), which is an algorithm based on time domain waveform inversions to search for the focal mechanism that best fits synthetic and observed waveforms. In the inversion procedure, the complete record is broken into two segments, the Pnl window and the surface wave window assigning different weights. When local *S* or teleseismic arrivals are not accessible, Pnl can be allowed to determine larger-scale local structures since it varies from the longer period Pn (0.33 Hz) to the shorter period Pg and PmP arrivals (0.5–2 Hz) in frequency contents (Savage & Helmberger, 2004). Pnl waves and surface waves mainly reflect crustal velocity structures and shallow structures, respectively (Zhu & Helmberger, 1996). The CAP method allows independent time shifts for the Pnl window and the surface wave window. This approach therefore ensures a more stable and robust inversion against imperfect velocity models (Zhu & Helmberger, 1996).

We calculate the corresponding Green's functions using a Haskell propagator matrix (fk) method (Zhu & Rivera, 2002), applying our best-estimated 1D velocity model for the Hutubi region. We similarly filter the

Table 1
Calculated Focal Mechanisms of Two Earthquakes Using the CAP Method

Event time	M_L	Frequency bands (Hz)	Strike/dip/slip (degree)	Focal depth (km)	M_w
20130803004922	3.0	0.1/0.4/0.05/0.12	Fault plane 1: 278/73/72 Fault plane 2: 146/25/135	3.9 ± 0.8	2.76
20130805080823	3.1	0.08/0.35/0.05/0.12	Fault plane 1: 307/73/90 Fault plane 2: 127/17/72	5.3 ± 0.9	3.02

synthetic and observed waveforms for individual events, slightly adjusting the filtering frequency bands for different events (Table 1). Then we minimize the misfit of each event through grid search to find the optimal source parameters (M_w, strike, dip, slip, and depth).

The CAP calculated dip angles of the M_w 3.0 (M_L 3.1) earthquake and M_w 2.8 (M_L 3.0) earthquake (fault plane 2 in Table 1; Figures 8a, 8d, and 9) are 17° and 25°, respectively, which agree well with the seismicity trend in depth section, estimated to around 20°. CAP inverted focal depth for the M_w 2.8 earthquake is 3.9 km (Figure 9c), consistent with hypoDD relocated depth. And the focal depth for the M_w 3.0 earthquake is 5.3 km by using the CAP method (Figure 9d), slightly deeper than the hypoDD relocated depth.

6. Discussion

The Hutubi UGS is located adjacent to a seismically active region, and frequent background earthquakes make it difficult to conclude that these earthquakes were inevitably induced by gas injection or extraction. The ETAS modeling and earthquake relocation results both suggest potential links between gas injection and two groups of seismicity during the first and second injection periods. Here we compare our results with those of previous studies and examine some factors that might have played a role in the injection-induced seismicity. We focus particularly on hypocenter distributions, focal depths, subsurface formations, source fault geometry, and well operation data. We then address the importance of establishing dedicated mobile networks near UGS sites and their critical influences in evaluating seismic hazards.

6.1. Supporting Evidence of Induced Seismicity Linked With Gas Injections

We classify the two groups of earthquakes occurring in August 2013 and May 2014 as anomalous seismicity in terms of very low background probability. Interestingly, we consistently relocate the anomalous seismicity, which was scattered tens of kilometers away in the initial catalog, to the vicinity of the Hutubi UGS. These two approaches independently suggest that the anomalous seismicity is associated with gas injection. The spatiotemporal correlation between seismicity and injection wells suggests a causal connection (Tang et al., 2018; Yang et al., 2017). Our results indicate that ETAS modeling correctly identify induced earthquake occurrences during the earlier two cycles in 2013 and 2014. While the seismicity is less clustered in time during cycles after 2015, it implies a lower stress perturbation (Mignan et al., 2018). If we focus on the north of the UGS, we may identify an increasing fraction of background seismicity with increasing injection time and a maximum magnitude earthquake occurring at a very early stage. Similar features have been found in wastewater-injection-induced seismicity on a depleted gas reservoir site (Lei et al., 2013).

6.2. Earthquake Relocations and the Fault Geometry
6.2.1. Location Improvements and Determined Focal Depths

The actual seismicity might far exceed that of the 167 events within our study region and study period, yet we could draw some implications from our more accurate relocations. Our hypoDD relocations sharpen the seismicity lineation and resolve focal depths much better for earthquakes near the Tien Shan Mountains and near the Hutubi UGS, separately (Figure 7b). Considering the very low background seismicity probabilities (Figures 4a and 5a) and the proximity to the Hutubi UGS (Figure 7b), we focus on the two event clusters that occurred in August 2013 and May 2014 (Figure 8a). The depths relocate around 3 to 4 km, close to the depths of the gas injection/extraction wells and slightly deeper than the reservoir formation (Figure 8d), suggesting inefficient gas diffusion to the overlying layers and certifying caprock integrity. Unlike injected water, injected gas is more buoyant and more likely to move upward where the overlying formation integrity is broken and a permeable channel is available. The poroelastic response of the injected zone is anticipated to be more similar for the cases of supercritical CO_2 and gaseous natural gas, by considering their viscosities and bulk moduli (Verdon, 2014). Moreover, both CO_2 and gas are less dense than in situ liquid (e.g., brine
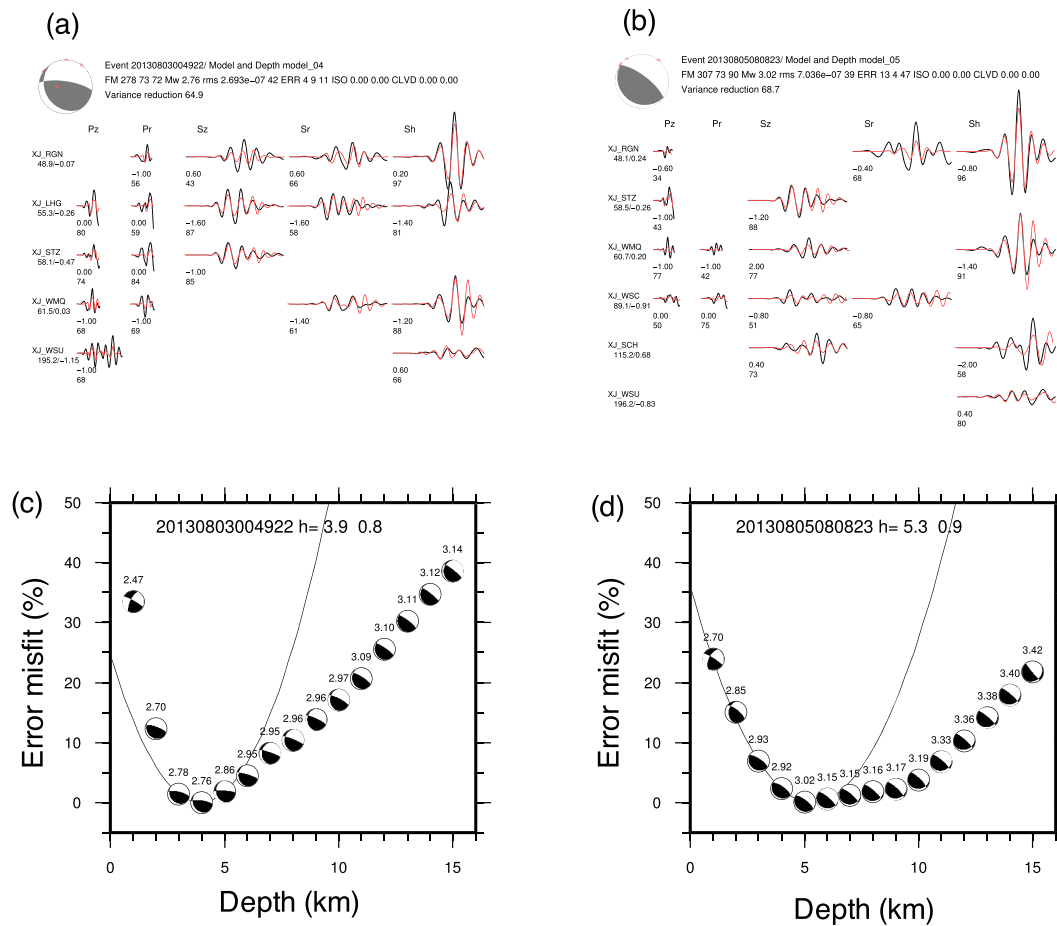
Figure 9. Waveform fittings and focal depths using CAP. (a and b) Waveform fittings (black, observation; red, synthetic) for the relocated M_L 3.0 (M_w 2.8) earthquake and M_L 3.1 (M_w 3.0) earthquake (Table 1). CAP derived optimal focal depths are shown in Figures 9c and 9d, respectively. The occurrence time, optimal focal depth, and depth error are labeled as texts (see Table 1). The gray line (Figures 9c and 9d) connecting the three beach balls around the minimum misfit is the fitted parabola to estimate the best focal depth. CAP = Cut and Paste.

water), therefore more likely to move upward wherever a permeable pathway is available. However, modeling results of CO_2 injection into faulted reservoirs indicate that induced earthquakes most likely occur beneath the reservoir formation instead of in the overlying layers (Rinaldi et al., 2014). Besides, we relocate no earthquakes within the reservoir volume, which itself might be very permeable, hindering excessive pressure accumulations (e.g., Lei et al., 2013).

Here we compare the results of earthquake locations and focal depths (see Figures 3, 8, and 9). Tang et al. (2018) relocated two groups of earthquakes near the Hutubi fault, close to the southern boundary of the UGS. The offsets between common earthquakes are about 6 and 3 km for the seismicity in August 2013 and May 2014, respectively. In addition, their depths significantly differ from ours: their depths are shallower than 2 km, likely above the caprock, while our depths are around 3 to 4 km. Two factors might contribute to this discrepancy. Tang et al.'s (2018) applied velocity model oversimplified the velocity structure above 20 km, limiting earthquake depth resolution and relocation accuracy. Their stations were also insufficiently close to the injection sites, the potential source region. Figure 3 shows the location discrepancies and the significant improvements made by incorporating mobile stations close to the source region, taking the same earthquake as an example.

In contrast to our results, Tang et al. (2018) relocated the earthquake depths to 2 km or shallower, likely above the caprock, implying that there had been a gas leakage into the low permeable cap rocks or the connected fault. Such occurrences are inefficient and unlikely. For the Hutubi fault, the upper plate Ziniquanzi formation has thicker mudstone thickness and increasing shale contents close to the fault plane,

encouraging sand mud to form on both sides of the fault and indicating a good fault sealing in the lateral direction (Pang et al., 2012). The H2002 well is located in the lower plate of the fault and used to produce gas, but the Hu003 well, in the upper plate of the fault and higher than the H2002 well, detected no oil and gas, further indicating that the Hutubi fault has a good lateral sealing (see Figure 8d, Pang et al., 2012).

6.2.2. Fault Geometry Implied From Focal Mechanism Solutions

Given the uncertainties of event locations and seismic velocity structures, it is often difficult to determine the focal mechanisms of small earthquakes. We use an alternative approach, examining and comparing the earthquake waveforms, on the assumption that closely spaced earthquakes with similar focal mechanisms should generate similar waveforms (e.g., Yang et al., 2009). To investigate whether the clustered events occurred on the same fault or not, we conduct waveform similarity analyses for the two groups of events recorded on the station STZ, in the light of its short distance from the source zone and its high-quality recordings (Figures 8b and 8c). Our location results indicate that the two groups of earthquakes are separated by ~5 km in distance (Figure 8a). While within each cluster the waveforms are nearly identical, waveforms at the same station are distinctly different from each other, suggesting that the relocated two grouped events occurred on two different faults with high resolution.

For the earthquake sequence in August 2013, the source fault is not hydrologically connected with the reservoir formation (Figures 8a and 8d). Qiao et al. (2018) and Tang et al. (2018) applied dip angles of around 80°, markedly different from the angles of 17° and 25° as we obtained in our calculations, and an estimated value of ~20° from geologic and seismic surveys (Cao, 2013; Pang et al., 2012). The overestimated dip angles may bias their simulation results for determining possible physical mechanisms for the induced seismicity and hence the seismic hazard assessment.

6.3. Responsible Mechanisms of Induced Seismicity Near the Hutubi UGS Facility

Both pore pressure increases and shear stress changes can cause fault failures (e.g., Bao & Eaton, 2016; Ellsworth, 2013; Zbinden et al., 2017). Thus, two end-member models are proposed considering the hydraulic connectivity between the fault and the permeable reservoir formation (e.g., Ellsworth, 2013). Our high-resolution earthquake locations indicate that a sequence of earthquakes in August 2013 occurred on a fault that is not hydrologically connected with the reservoir formation. Consequently, the fault is unlikely to have been pore pressure diffused.

We also consider well operation data including wellhead pressure, injection rate, and total injection volume (see Tang et al., 2018). The largest M_w 3.0 earthquake occurred when the wellhead pressure reached 24 MPa, smaller than the peak pressure of 28 MPa. We observe no fast response of surging seismicity to wellhead pressure changes or vice versa. The well injection data in the time display multipoint sharp changes of wellhead pressure and gas injection rate. But correlated induced seismicity is concentrated both in time and space during the first two cycles, with no significant earthquake occurrences after the shutdowns of the injection well and during the gas extraction periods (see Tang et al., 2018). More than 4 billion m^3 of gas was compressed into the reservoir formation between June 2013 and December 2015. And the accumulated injection volume increases by about 1.5 billion m^3 each year. But very few earthquakes close to the injection sites have been observed since 2016 (see Figure 5a). Therefore, we argue that pore pressure changes resulting in a lowering of the effective normal stress is unlikely to have been the dominant mechanism inducing earthquakes in our study region and study period. This indicates that poroelasticity in a critically stressed crust could be an alternative mechanism. We speculate that slowly transitioning from undrained to a drained response resulted in lower stress perturbation that would contribute to the waning seismic response after the second round of injection.

Tang et al. (2018) relocated earthquake depths shallower than 2 km and attributed fault failures on nearby faults to both pore pressure changes and poroelastic responses, governed by the rate- and state-dependent friction law (Dieterich, 1979). However, their relocated depths are above impermeable cap rocks, and gas would not have diffused upward in such circumstances. Furthermore, velocity strengthening (aseismic) behavior is often found in frictional experiments at shallow depths (Blanpied et al., 1998), in contrast to their observations in the Hutubi UGS region. Although shallow velocity strengthening patches may break during large ruptures as shown in numerical simulations (e.g., Yang et al., 2012; Yu et al., 2018), it is not anticipated that such regions would be seismically active. If indeed heterogeneous small velocity-weakening patches are

surrounded by the aseismic/creeping section, such as the Parkfield section of the San Andreas fault, repeating earthquakes are likely observed. However, that is not the case near the Hutubi UGS.

6.4. Seismic Hazard Assessments Near the Hutubi UGS Facility

The observed anomalous seismicity is more likely to have been induced by gas injection perturbated poroelastic stress. Instead of gas injection parameters, the size and stress state of the fault would control the largest magnitude of the induced earthquakes. In this respect, it should be noted that a fault of a few kilometers in length is quite capable of producing $M5$ or larger earthquakes. More importantly, continuing gas injection might increase the likelihood of reactivating critical faults at certain distances from the UGS. Therefore, the survey of fault sizes, fault distributions, and fault geometries plays a key role in the hazard assessments of induced seismicity (Lei et al., 2013).

Tang et al. (2018) overestimated the fault dip angle in their numerical modeling approaches. They lacked focal mechanism solution constraints and documented seismic surveyed evidence as we had. It is likely that their modeled Coulomb stress patterns would have changed significantly if they had applied a dip angle of around 20°.

We believe that it is necessary to carefully investigate preexisting faults prior to injection, aiming to reduce the possibility that any mapped large fault nearby is critical for failure. Since we have little knowledge of the stress conditions on mapped faults, a safe approach is to avoid that any mapped large fault is located within a respect distance (e.g., ~10 km). More importantly, engineers and seismologists should be required to conduct real-time monitoring of seismicity and reliable earthquake locations during injections. Such precautions would provide useful and timely information and would help to ensure the safe running of UGS facilities.

Many induced seismicity projects utilize the local seismic network in the activated areas, but the new stations are usually deployed after the initiation of seismicity. Consequently, the network geometry is often unfavorable for resolving the underlying fault structures. By contrast, our newly deployed mobile network went into operation before the Hutubi UGS facility opened. We have shown that earthquake locations can be more accurately determined by using at least one or two mobile stations close to injection sites (see Figure 3). We could probably have captured features of earlier stage seismicity if we had not suffered from significant data gaps. Comparisons with seismicity induced by wastewater or CO_2 injections may also provide potential insights into seismicity linked with UGS facilities and the consequential seismic hazards (Verdon, 2014; Zbinden et al., 2017).

7. Conclusions

Both our ETAS modeled results and our high-resolution relocations suggest gas-injection-induced seismicity adjacent to the Hutubi UGS during the first and second injection periods. We examined induced seismicity correlations with geological formations, source fault geometry, and well injection data. Our seismological investigation results indicate that these on-fault earthquakes were not hydrologically connected with the reservoir formation. Therefore, we argue that the induced seismicity was instead caused by poroelastic stress perturbations due to the gas injection. Moreover, we highlight the importance of establishing a dedicated mobile network near UGS sites because of its critical influence on seismic hazard assessments.

References

Atkinson, G. M., Eaton, D. W., Ghofrani, H., Walker, D., Cheadle, B., Schultz, R., et al. (2016). Hydraulic fracturing and seismicity in the Western Canada Sedimentary Basin. *Seismological Research Letters*, *87*(3), 631–647. https://doi.org/10.1785/0220150263

Bao, X., & Eaton, D. W. (2016). Fault activation by hydraulic fracturing in western Canada. *Science*, *354*(6318), 1406–1409. https://doi.org/10.1126/science.aag2583

Blanpied, M. L., Marone, C. J., Lockner, D. A., Byerlee, J. D., & King, D. P. (1998). Quantitative measure of the variation in fault rheology due to fluid-rock interactions. *Journal of Geophysical Research*, *103*(B5), 9691–9712. https://doi.org/10.1029/98JB00162

Cao, X. (2013). *A research on reservoir geomechanical features of a gas storage in Xinjiang after natural depletion (in Chinese). Ph.D. Thesis*. Beijing: China University of Geosciences (Beijing).

Cesca, S., Grigoli, F., Heimann, S., González, Á., Buforn, E., Maghsoudi, S., et al. (2014). The 2013 September-October seismic sequence offshore Spain: A case of seismicity triggered by gas injection? *Geophysical Journal International*, *198*(2), 941–953. https://doi.org/10.1093/gji/ggu172

Chen, W., Yu, P., Xiong, W., Li, J., Feng, G., & Qiao, X. (2016). InSAR deformation monitoring and simulation of Hutubi underground gas storage in Xinjiang (in Chinese). *Geodesy and Geodynamics*, *36*(09), 803–807.

Chen, X., Haffener, J., Goebel, T. H. W., Meng, X., Peng, Z., & Chang, J. C. (2018). Temporal correlation between seismic moment and injection volume for an induced earthquake sequence in Central Oklahoma. *Journal of Geophysical Research: Solid Earth*, *123*, 3047–3064. https://doi.org/10.1002/2017JB014694

Chen, Y., Wang, B., & Yao, H. (2017). Seismic airgun exploration of continental crust structures. *Science China Earth Sciences*, *60*(10), 1739–1751. https://doi.org/10.1007/s11430-016-9096-6

Deng, Q., Zhang, P., Ran, Y., Yang, X., Min, W., & Chen, L. (2003). Active tectonics and earthquake activities in China (in Chinese). *Earth Science Frontiers*, *10*(S1), 66–73.

Dieterich, J. H. (1979). Modeling of rock friction 1. Experimental results and constitutive equations. *Journal of Geophysical Research*, *84*(B5), 2161–2168. https://doi.org/10.1029/JB084iB05p02161

Ellsworth, W. L. (2013). Injection-induced earthquakes. *Science*, *341*(6142), 1225942. https://doi.org/10.1126/science.1225942

Foulger, G. R., Wilson, M. P., Gluyas, J. G., Julian, B. R., & Davies, R. J. (2018). Global review of human-induced earthquakes. *Earth-Science Reviews*, *178*, 438–514. https://doi.org/10.1016/j.earscirev.2017.07.008

Galis, M., Ampuero, J. P., Mai, P. M., & Cappa, F. (2017). Induced seismicity provides insight into why earthquake ruptures stop. *Science Advances*, *3*(12), eaap7528. https://doi.org/10.1126/sciadv.aap7528

Grigoli, F., Cesca, S., Priolo, E., Rinaldi, A. P., Clinton, J. F., Stabile, T. A., et al. (2017). Current challenges in monitoring, discrimination, and management of induced seismicity related to underground industrial activities: A European perspective. *Reviews of Geophysics*, *55*, 310–340. https://doi.org/10.1002/2016RG000542

Guan, S., Chen, F., & Fang, S. (2012). Three potential exploration areas of Southern Junggar Basin, NW China: Arguments from structural modeling. *Petroleum Exploration and Development*, *39*(1), 43–50. https://doi.org/10.1016/S1876-3804(12)60013-5

Healy, J. H., Rubey, W. W., Griggs, D. T., & Raleigh, C. B. (1968). The Denver earthquakes. *Science*, *161*(3848), 1301–1310. https://doi.org/10.1126/science.161.3848.1301

Holland, A. A. (2013). Earthquakes triggered by hydraulic fracturing in south-central Oklahoma. *Bulletin of the Seismological Society of America*, *103*(3), 1784–1792. https://doi.org/10.1785/0120120109

Hu, G., Zhang, S., Li, J., Li, J., & Han, Z. (2010). The origin of natural gas in the Hutubi gas field, southern Junggar foreland sub-basin, NW China. *International Journal of Coal Geology*, *84*(3–4), 301–310. https://doi.org/10.1016/j.coal.2010.10.009

Ji, Z., Wang, B., Wang, H., Wang, Q., & Su, J. (2017). Seismic velocity and its temporal variations of Hutubi basin revealed by near surface trapped waves. Paper presented at 2017 AGU Fall Meeting, American Geophysical Union, New Orleans, Louisiana.

Jia, K., Zhou, S., Zhuang, J., Jiang, C., Guo, Y., Gao, Z., & Gao, S. (2018). Did the 2008 Mw 7.9 Wenchuan earthquake trigger the occurrence of the 2017 Mw 6.5 Jiuzhaigou earthquake in Sichuan, China? *Journal of Geophysical Research: Solid Earth*, *123*, 2965–2983. https://doi.org/10.1002/2017JB015165

Jiang, G., Liu, L., Yang, H., & Wong, T.F. (2019). Ground expansion and seismic hazard induced by the Hutubi natural gas repository, Xinjiang, China. Paper presented at the third Schatzalp Workshop on Induced Seismicity, the Swiss Seismological Service at ETH Zurich, Davos, Switzerland.

Juanes, R., Castiñeira, D., Fehler, M. C., Hager, B. H., & Shaw, J. H. (2017). Coupled flow and geomechanical modeling, and assessment of induced seismicity, at the Castor Underground Gas Storage Project. Final Report, 1–86.

Keranen, K. M., Savage, H. M., Abers, G. A., & Cochran, E. S. (2013). Potentially induced earthquakes in Oklahoma, USA: Links between wastewater injection and the 2011 M_w 5.7 earthquake sequence. *Geology*, *41*(6), 699–702. https://doi.org/10.1130/G34045.1

Keranen, K. M., & Weingarten, M. (2018). Induced seismicity. *Annual Review of Earth and Planetary*, *46*(1), 149–174. https://doi.org/10.1146/annurev-earth-082517-010054

Klein, F. W. (2002). User's guide to HYPOINVERSE-2000, a Fortran program to solve for earthquake locations and magnitudes: USGS Open File Report 02-171. https://doi.org/http://geopubs.wr.usgs.gov/open-file/of02-171/

Lei, X., Ma, S., Chen, W., Pang, C., Zeng, J., & Jiang, B. (2013). A detailed view of the injection-induced seismicity in a natural gas reservoir in Zigong, southwestern Sichuan basin, China. *Journal of Geophysical Research: Solid Earth*, *118*, 4296–4311. https://doi.org/10.1002/jgrb.50310

Li, J., Zhang, J., Zhao, X., Jiang, M., Li, Y., Zhu, Z., et al. (2016). Mantle subduction and uplift of intracontinental mountains: A case study from the Chinese Tianshan Mountains within Eurasia. *Scientific Reports*, *6*(1), 28831. https://doi.org/10.1038/srep28831

Lu, R., He, D., Xu, X., Wang, X., Tan, X., & Wu, X. (2017). Seismotectonics of the 2016 *M* 6.2 Hutubi earthquake: Implications for the 1906 *M* 7.7 Manas earthquake in the Northern Tian Shan belt, China. *Seismological Research Letters*, *89*(1), 13–21. https://doi.org/10.1785/0220170123

Marone, C. (1998). Laboratory-derived friction laws and their application to seismic faulting. *Annual Review of Earth and Planetary Sciences*, *26*(1), 643–696. https://doi.org/10.1146/annurev.earth.26.1.643

McGarr, A. (2014). Maximum magnitude earthquakes induced by fluid injection. *Journal of Geophysical Research: Solid Earth*, *119*, 1008–1019. https://doi.org/10.1002/2013JB010597

Mignan, A., Danciu, L., & Giardini, D. (2018). Considering large earthquake clustering in seismic risk analysis. *Natural Hazards*, *91*(Suppl 1), 149–172. https://doi.org/10.1007/s11069-016-2549-9

Ogata, Y. (1998). Space-time point-process models for earthquake occurrences. *Annals of the Institute of Statistical Mathematics*, *50*(2), 379–402. https://doi.org/10.1023/A:1003403601725

Ogata, Y., & Zhuang, J. (2006). Space-time ETAS models and an improved extension. *Tectonophysics*, *413*(1–2), 13–23. https://doi.org/10.1016/j.tecto.2005.10.016

Pang, J., Qian, G., Wang, B., Yang, Z., Wei, Y., & Li, Y. (2012). Evaluation of sealing ability of underground gas storage converted from the Xinjiang H gas field (in Chinese). *Natural Gas Industry*, *32*(2), 83–85.

Qiao, X., Wei, C., Dijin, W., Zhaosheng, N., Zhengsong, C., Jie, L., et al. (2018). Crustal deformation in the Hutubi underground gas storage site in China observed by GPS and InSAR measurements. *Seismological Research Letters*, *89*(4), 1467–1477. https://doi.org/10.1785/0220170221

Raleigh, C. B., Healy, J. H., & Bredehoeft, J. D. (1976). An experiment in earthquake control at Rangely, Colorado. *Science*, *191*(4233), 1230–1237. https://doi.org/10.1126/science.191.4233.1230

Rinaldi, A. P., Rutqvist, J., & Cappa, F. (2014). Geomechanical effects on CO_2 leakage through fault zones during large-scale underground injection. *International Journal of Greenhouse Gas Control*, *20*, 117–131. https://doi.org/10.1016/j.ijggc.2013.11.001

Savage, B., & Helmberger, D. (2004). Site response from incident Pnl waves. *Bulletin of the Seismological Society of America*, *94*(1), 357–362. http://resolver.caltech.edu/CaltechAUTHORS:20140801-091627948, https://doi.org/10.1785/0120030145

Segall, P. (1989). Earthquakes triggered by fluid extraction. *Geology*, *17*(10), 942–946. https://doi.org/10.1130/0091-7613(1989)017<0942:ETBFE>2.3.CO;2

Seif, S., Mignan, A., Zechar, J., Werner, M., & Wiemer, S. (2017). Estimating ETAS: The effects of truncation, missing data, and model assumptions. *Journal of Geophysical Research: Solid Earth*, *122*, 449–469. https://doi.org/10.1002/2016JB012809

Suckale, J. (2009). Induced seismicity in hydrocarbon fields. *Advances in Geophysics*, *51*(C), 55–106. https://doi.org/10.1016/S0065-2687(09)05107-3

Sun, A., Chen, Q., Chen, Y., Li, G., & Zhang, Z. (2012). Relocation of earthquakes in the northeastern Tianshan Mountains area and improvement of local 1-dimensional crustal velocity model. *Earthquake Research in China*, *26*(3), 321–344.

Tang, L., Lu, Z., Zhang, M., Sun, L., & Wen, L. (2018). Seismicity induced by simultaneous abrupt changes of injection rate and well pressure in Hutubi gas field. *Journal of Geophysical Research: Solid Earth*, *123*, 5929–5944. https://doi.org/10.1029/2018JB015863

Tang, L., Zhang, M., Sun, L., & Wen, L. (2015). Injection-induced seismicity in a natural gas reservoir in Hutubi, southern Junggar basin, northwest China. Paper presented at 2015 AGU Fall Meeting, American Geophysical Union, San Francisco, California.

Tang, L., Zhang, M., & Wen, L. (2017). Source discrimination between mining blasts and earthquakes in Tianshan orogenic belt, NW China. Paper presented at 2017 AGU Fall Meeting, American Geophysical Union, New Orleans, Louisiana.

Verdon, J. P. (2014). Significance for secure CO_2 storage of earthquakes induced by fluid injection. *Environmental Research Letters*, *9*(6). https://doi.org/10.1088/1748-9326/9/6/064022

Waldhauser, F., & Ellsworth, W. L. (2000). A double-difference earthquake location algorithm: Method and application to the Northern Hayward Fault, California. *Bulletin of the Seismological Society of America*, *90*(6), 1353–1368. https://doi.org/10.1785/0120000006

Wang, J., Yao, H., Wang, W., Wang, B., Li, C., Wei, B., & Feng, L. (2018). Study of the near-surface velocity structure of the Hutubi gas storage area in Xinjiang from ambient noise tomography (in Chinese). *Chinese Journal of Geophysics*, *61*(11), 4436–4447. https://doi.org/10.6038/cjg2018M0025

Wiemer, S. (2001). A software package to analyze seismicity: ZMAP. *Seismological Research Letters*, *72*(3), 373–382. https://doi.org/10.1785/gssrl.72.3.373

Wiemer, S., & Wyss, M. (2000). Minimum magnitude of completeness in earthquake catalogs: Examples from Alaska, the Western United States, and Japan. *Bulletin of the Seismological Society of America*, *90*(4), 859–869. https://doi.org/10.1785/0119990114

Wilson, M. P., Foulger, G. R., Gluyas, J. G., Davies, R. J., & Julian, B. R. (2017). HiQuake: The human-induced earthquake database. *Seismological Research Letters*, *88*(6), 1560–1565. https://doi.org/10.1785/0220170112

Yang, H. (2015). Recent advances in imaging crustal fault zones: A review. *Earthquake Science*, *28*(2), 151–162. https://doi.org/10.1007/s11589-015-0114-3

Yang, H., Liu, Y., & Lin, J. (2012). Effects of subducted seamounts on megathrust earthquake nucleation and rupture propagation. *Geophysical Research Letters*, *39*, L24302. https://doi.org/10.1029/2012GL053892

Yang, H., Liu, Y., Wei, M., Zhuang, J., & Zhou, S. (2017). Induced earthquakes in the development of unconventional energy resources. *Science China Earth Sciences*, *60*(9), 1632–1644. https://doi.org/10.1007/s11430-017-9063-0

Yang, H., Zhu, L., & Chu, R. (2009). Fault-plane determination of the 18 April 2008 Mount Carmel, Illinois, earthquake by detecting and relocating aftershocks. *Bulletin of the Seismological Society of America*, *99*(6), 3413–3420. https://doi.org/10.1785/0120090038

Yu, H., Liu, Y., Yang, H., & Ning, J. (2018). Modeling earthquake sequences along the Manila subduction zone: Effects of three-dimensional fault geometry. *Tectonophysics*, *733*, 73–84. https://doi.org/10.1016/j.tecto.2018.01.025

Zbinden, D., Rinaldi, A. P., Urpi, L., & Wiemer, S. (2017). On the physics-based processes behind production-induced seismicity in natural gas fields. *Journal of Geophysical Research: Solid Earth*, *122*, 3792–3812. https://doi.org/10.1002/2017JB014003

Zhao, L., & Helmberger, D. (1994). Source estimation from broadband regional seismograms. *Bulletin of the Seismological Society of America*, *84*(1), 91–104.

Zheng, X., Yao, Z., Liang, J., & Zheng, J. (2010). The role played and opportunities provided by IGP DMC of China National Seismic Network in Wenchuan earthquake disaster relief and researches. *Bulletin of the Seismological Society of America*, *100*(5B), 2866–2872. https://doi.org/10.1785/0120090257

Zhu, L., & Helmberger, D. (1996). Advancement in source estimation techniques using broadband regional seismograms. *Bulletin of the Seismological Society of America*, *86*(5), 1634–1641.

Zhu, L., & Rivera, L. A. (2002). A note on the dynamic and static displacements from a point source in multilayered media. *Geophysical Journal International*, *148*(3), 619–627. https://doi.org/10.1046/j.1365-246X.2002.01610.x

Zhuang, J., Chang, C. P., Ogata, Y., & Chen, Y. I. (2005). A study on the background and clustering seismicity in the Taiwan region by using point process models. *Journal of Geophysical Research*, *110*, B05S18. https://doi.org/10.1029/2004JB003157

Zhuang, J., Ogata, Y., & Vere-Jones, D. (2002). Stochastic declustering of space-time earthquake occurrences. *Journal of the American Statistical Association*, *97*(458), 369–380. https://doi.org/10.1198/016214502760046925